Stable Coexistence of Spiral and Target Patterns in Freely Suspended Films of Smectic-*C* Liquid Crystals

P. E. Cladis,[1] P. L. Finn,[1] and Helmut R. Brand[2]
[1]*AT&T Bell Laboratories, Murray Hill, New Jersey 07974*
[2]*Theoretische Physik III, Universität Bayreuth, D 95440 Bayreuth, Federal Republic of Germany*
(Received 29 November 1994; revised manuscript received 1 May 1995)

We have observed the stable coexistence of target and spiral patterns in thick freely suspended films of a smectic-*C* liquid crystal in a rotating electric field. In this system, patterns arise from a competition between boundary effects and bulk electric field torques and show a simple connection between spiral and target dynamics. We compare our observations in this driven system with experimental reports of spirals and targets in nonequilibrium systems such as large aspect ratio Bénard convection.

PACS numbers: 47.20.–k, 05.70.Ln, 61.30.–v

Over the last few years, pattern formation in spatially extended driven systems has been a rapidly growing subfield of nonequilibrium physics [1–3]. Following earlier observations of spirals in nonequilibrium systems as diverse as autocatalytic chemical reactions [4] and thermal convection [5], among the fascinating phenomena recently observed are spiral chaos [6] and the chaotic coexistence of spirals and targets [7] in large aspect ratio Bénard convection.

Here we present observations of a pattern forming system, driven by a rotating electric field, where boundary topology can change from one compatible with a target pattern [Fig. 1(a)] to one favoring a spiral pattern [Fig. 1(c)]. The transition from target to spiral is mediated by a novel stable spiral-target bound state with the target acting as a phase sink and the spiral a phase source. The *stable* coexistence of a target and a spiral [Fig. 1(b)], never before observed in other pattern forming systems, reveals a simple connection between target and spiral dynamics.

As the rotating electric field gives these patterns a handedness the system does not have in its absence, this study complements earlier ones on patterns formed at interfaces in intrinsically chiral materials [8–10]. Targets and spirals are also prevalent when a mechanical torque is applied to freely suspended smectic-*C* films [11–13], the large radius ratio analog of the Taylor instability studied in nematic liquid crystals [14]. In previous experiments involving liquid crystals and rotating electric fields (frequency $\nu = 10$–100 Hz, aspect ratio $\Gamma = R/d \sim 1000$ with radius R and film thickness d), only targets have been observed in thin films ($d < 1$ μm) of chiral smectic liquid crystals [15,16] while spirals (but no targets) are observed in nematic liquid crystals in a rotating magnetic field ($\nu = 1$ Hz, $\Gamma \sim 135$) [17].

The closest similarity between observations reported here appears in cylindrical, large aspect ratio ($\Gamma \sim 80$) Rayleigh-Bénard convection in CO_2 gas under pressure [4]: the transition from hexagons to rolls involves n-armed spirals (with $0 > n \geq 13$) and n phase dislocations orbiting the spiral. In that system [5], a defect-free boundary condition prevails. In terms of a topological index S, this is the $S = 0$ condition (Fig. 2). In our system ($50 < \Gamma < 200$), a large enough applied electric field can change boundary topology from, e.g., $S = 0$ (target) to $S = 1$ (spiral) by dragging in defects from the edge of the film (Fig. 2). While we have also observed dynamic states that conserve boundary topology, e.g., a steady-state spiral ($S = 1$) at the film center with a single orbiting defect ($S = -1$) mediating the transition from spiral back to target pattern, and even stationary double spirals ($S = 2$) [18], here we focus on the novel, steady-state, defect-target bound state [Fig. 1(b)] mediating the transition from a target [$S = 0$, Fig. 1(a)] to a centered spiral [$S = 1$, Fig. 1(c)].

Patterns in Fig. 1 are observed in thick (thickness $10 \geq d \geq 18$ μm), freely suspended films of a smectic-*C* liquid crystal. Smectic *C* is a layered system with in-plane anisotropic fluidity characterized by a unit vector $\mathbf{c} = (\cos\Phi, \sin\Phi)$ [11], where Φ is the angle between $\mathbf{c}(r)$ at any location r in the film and $\mathbf{c}(R)$. Film geometries suppress dynamic couplings to layer structures and highlight the spatiotemporal behavior of $\mathbf{c}$. Additional advantages are accessibility to observations in a polarizing microscope (where lines of constant Φ are rings in target patterns and spirals when associated with defects) and convenient time scales (seconds to minutes). While qualitatively similar to a two-dimensional nematic, about which a great deal is known, an important difference is that $\mathbf{c}$ and $-\mathbf{c}$ are not equivalent. As a result, defects in the orientation of $\mathbf{c}$ are characterized by integer numbers for the topological index S (Fig. 2).

A circular freely suspended film (radius $R \sim 1$ mm) of 10E6 (4′-hexyloxyphenyl 4-decyloxybenozate) in the smectic-*C* phase (temperature, 73.1 °C [19]) is prepared so that at rest it is free of defects in $\mathbf{c}$ ($\Phi \approx$ const), the simplest $S = 0$ topological state. The film thickness d is estimated by measuring the separation of 45° incident light when reflected from the top and bottom film surfaces [20]. Here $d \approx 13.5$ μm. Γ determines the total number of rings with larger Γ films having more rings.

Two pairs of flat electrodes (each 1.27 mm wide and 70 μm thick) are positioned (Fig. 1) around the film.

 0031-9007/95/75(8)/1518(4)$06.00

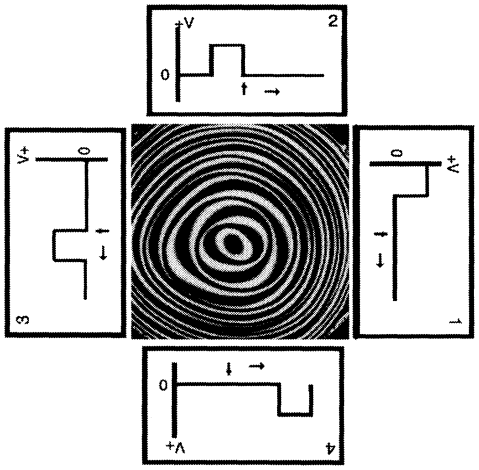

(a)

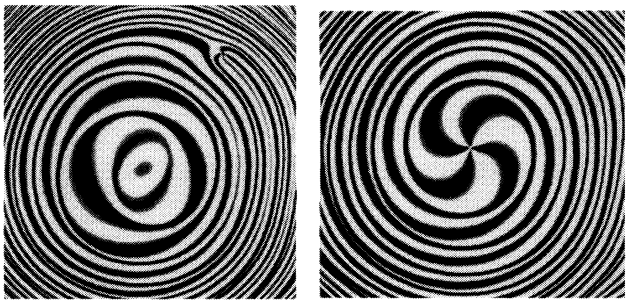

(b) (c)

FIG. 1. Basic steady-state patterns observed in thick freely suspended smectic-C films in a rotating electric potential U, $40 \lesssim U \lesssim 240$ V. Polarizer and analyzer are crossed parallel to the electrodes. (a) Experimental setup showing the electrode configuration and the applied voltage pulses: for a counterclockwise rotation, pulses applied to terminals 1 and 3 are $-90°$ out of phase with those to terminals 2 and 4. For the target state shown in the setup $d = 16$ μm, $U = 70$ V and scale, 1.3 mm (vertical) $\times$ 1.4 mm (horizontal). (b) Coexistence of an orbiting $S = +1$ defect and a target. The defect rotation sense is here counterclockwise, the same as the applied rotating field. A 2π rotation of the defect generates 2π more phase then propagates to the film center and is annihilated by the target: the target acts as a phase sink and the defect as a phase source. $d = 17$ μm, $U = 90$ V. the radial distance between the target center and the orbiting defect is 0.58 mm. (c) The $S = +1$ spiral ($U = 60$ V, $d = 17$ μm) with the orbiting defect in (b) at the film center. Same magnification as (b).

The separation between opposing electrodes is 2.3 mm. Four mercury switches direct a dc voltage U ($10 < U < 300$ V) to electrodes marked 1, 2, 3, and 4 in Fig. 1(a). The decay time of the applied voltage is ~ 95 μs and its rise time about 10 times faster. While here $\nu = 2.6$ Hz, the patterns' spatial and temporal scales are determined by sample geometry and material constants.

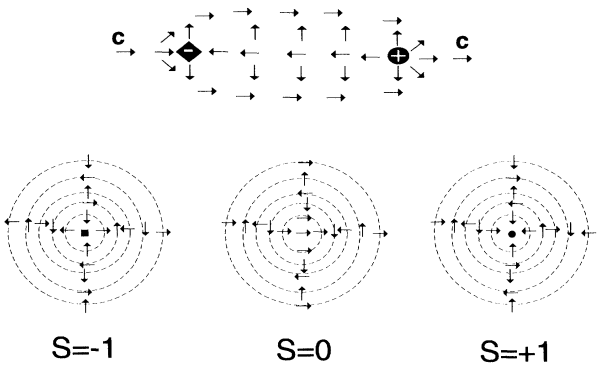

FIG. 2. Schematic drawing of the $\mathbf{c}$ field for an $S = +1$ and $S = -1$ defect pair (top). In the experiment, a single defect acts as a 2π phase dislocation in a ring pattern. A rotating defect can either create or destroy phase depending on the sense of its rotation. Schematic plots of $S = -1$, $S = 0$, and $S = +1$ (bottom) showing their different topologies and accounting for the contrast between crossed polarizers characteristic of a target [Fig. 1(a)] and a centered spiral [Fig. 1(c)].

Apart from length scales R and d associated with film geometry, a third length, the electric field coherence length, is $\xi_E = (4\pi K/\epsilon_c)^{1/2}/E$, where K is an elastic constant and ϵ_c is the dielectric anisotropy in the plane of the layers. As $E\xi_E$ is a material constant, two threshold fields can be defined when $\xi_{E_1} \sim R$ and $\xi_{E_2} \sim d$, i.e., $E_2/E_1 \propto \Gamma$.

The temporal scale for these patterns is set by the orientational diffusion constant defined as $D_0 = K/\gamma_1$, where γ_1 is the in-plane rotational viscosity. By observing the phase relaxation at 73.1 °C when the field is turned off [11], we find $D_0 = 9.5 \times 10^{-5}$ cm^2/s, independent of d.

When $U_c \sim 40$ V, four dark rings (corresponding to a 2π rotation of $\mathbf{c}$) formed. With no defects in the film, when $U > U_c$, a target pattern resulted that eventually reached a stationary maximum phase $\Phi_{\max} \propto U - U_c$, i.e., a maximum number of rings.

Figure 3 shows a remarkable result: The radial phase distributions of target patterns for four different voltages $U = 80, 100, 130$, and 160 V lie on a universal curve when the observed phase Φ is scaled by $\Phi_{\max}$ and its radius by R. There are three regimes: a boundary layer adjacent to the outer rim ($r > 0.88R = R^*$), a parabolic "inside" driving regime ($r < R_1$), where R_1 is to be determined, and a linear "buffer" ($R^* > r > R_1$), where elastic energy generated at $r = 0$ is stored. Matching the inside parabolic regime with the linear buffer by continuity of $d\Phi/dr$ at R_1 gives $R_1 = 0.51R$. At $r = R_1$, $\Phi = 0.6\Phi_{\max}$: more than half the rings are in the buffer. The unscaled data for $\Phi_{\max}$ and $d\Phi/dr$ show that R, can be determined only above a threshold voltage. From the inset in Fig. 3, we estimate this threshold to be $U = 50$ V.

The target pattern is stable with increasing voltage until $U \approx 120$ V ($d = 13.5$ μm), when a defect appears at the

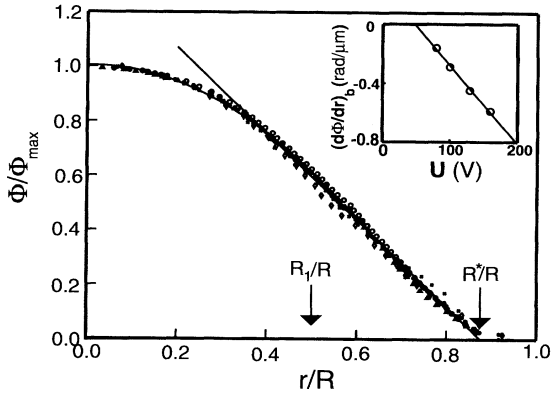

FIG. 3. Scaled radial phase distribution of target patterns obtained for four voltages [$U = 80$ (■), 100 (◇), 130 (△), and 160 V (○)] by digitizing captured video frames (film thickness $d = 13.5$ μm) along a line $\phi \sim \pi/4$. The smoothed average of all the data (solid circles) fit the linear buffer region by $\Phi/\Phi_{\max} = 1.4 - 1.52(r/R)$ and the parabolic inside region by $\Phi/\Phi_{\max} = 1.0 - 0.028(r/R) - 1.45(r/R)^2$. The unscaled data for $\Phi_{\max}$ an the slope in the buffer region $(d\Phi/dr)_b$ (shown inset) are linear in U and are used to determine U_c.

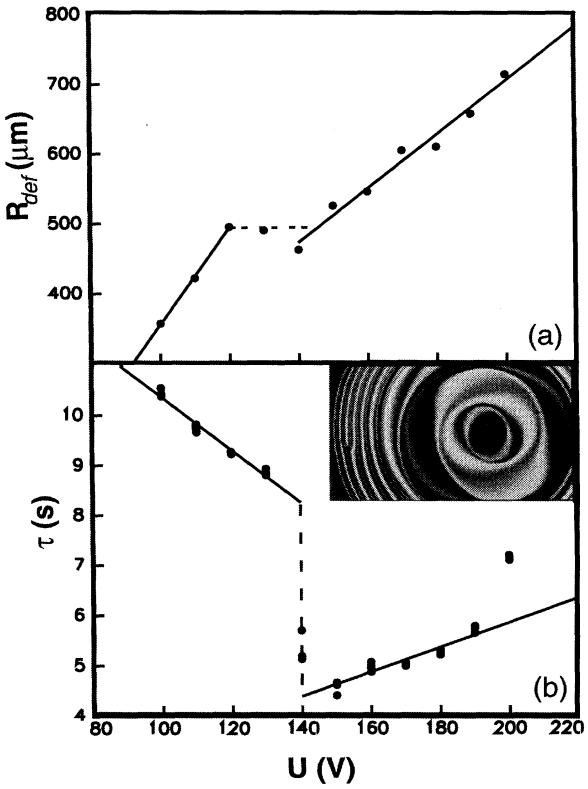

FIG. 4. (a) The orbit radius $R_{\rm def}$ and (b) the orbit time τ of the stationary bound state of an orbiting defect ($S = +1$) and target sink as a function of the applied voltage U. Inset in (b), a video frame of this stationary state shows only $\sim 2\pi$ phase in the inside region when $d = 13.5$ μm, $\nu = 2.6$ Hz, and $U = 200$ V. At $U = 240$ V, there is a transition to a chaotic state.

film edge rotating as a phase sink for phase generated by the target. When it first appears, the defect forms a spiral ending in the inside region and the pattern is temporally ordered as a phase creation by the target is exactly annihilated by the orbiting $S = +1$. With increasing field, the defect moves to smaller r. When it arrives at $r = 0$, it exchanges roles with the target, then moves away from $r = 0$ to orbit the target creating 2π phase with each rotation [Figs. 1(b) and 4(b)]. Now the $S = +1$ spiral ends at R: The boundary topology has changed from $S = 0$ to $S = 1$.

Both the defect's orbit radius $R_{\rm def}$ [Fig. 4(a)] and its time for a 2π rotation τ [Fig. 4(b)] change with applied field $R_{\rm def}$ being closer to the target center in lower fields. Figure 4(b) shows a narrow transition region at $U = 140$ V when $R_{\rm def} \approx R/2$. This is the boundary between the defect-target bound state inside and buffer regions. As the defect approaches the center, its time for a 2π rotation increases eventually resulting in a stationary centered spiral pattern at $r = 0$ [Fig. 1(c)].

Unlike centered spirals in large aspect ratio convection [5], this spiral does not emit phase consistent with the absence of rotating phase dislocations and a topological transition to $S = 1$ boundary conditions. Space-time plots through the spiral center (17 μm) show a 10 V reduction in voltage results in a 2π phase loss in the spiral arms: Phase propagates radially towards the defect core where it is annihilated resulting in a spiral with one less turn. When $U \approx 20$ V there are no more turns in the spiral. At $U = 0$, the defect may wander off center, but it does not disappear, more evidence that boundary conditions have changed.

At large fields ($U \geq 240$ V), the defect orbit is close to the film edge and eventually pulls in other defects. When this is a single $S = -1$, the pair migrates to the film center with chaotic dynamics to eventually annihilate. There is then a transition to a regular blinking state at a frequency comparable to the applied frequency indicating strong coupling to sufficiently high fields [18].

Inside and buffer responses are observed for τ. In Fig. 4(b), the defect speed in the buffer is approximately constant: $v^b_{\rm def} = 706 \pm 45$ μm/s. As $D_0/d = 709$ μm/s, we conclude that buffer dynamics is dominated by film thickness. When the rotation sense of the external field is changed from counterclockwise to clockwise, the $S = +1$ orbit also changes as, in this system, handedness is externally imposed.

We believe the bound defect-target pair to be the most interesting state so far observed: While topologically distinct from each other, they are a robust steady-state source-sink pair cooperating over long distances. Their steady-state properties have been checked for 16 h, a long time in a system where the longest characteristic time,

the director diffusion time, is $R^2/D_0 \sim 10^2$ s. 16 h in this system corresponds to weeks in [5]. This state exists over a wide range of voltages (Fig. 4) and there is no measurable hysteresis in its transition from centered spiral to defect-target bound state. Because of its long range spatiotemporal coherence, it contrasts with convection where chaotic spirals and targets coexist [7] and is qualitatively similar to rotating spiral or defects observed in [5]. Differences between this system and the latter are that, here, handedness is externally imposed, the boundary topology can change, and time scales are much shorter.

In conclusion, we have described observations in freely suspended thick films of smectic-C liquid crystals and quantitatively characterized a novel stationary state that consists of a defect (spiral) orbiting a target. The target and spiral act as complementary and interchangeable phase source or sink depending on boundary conditions and the applied field. In the case of target patterns, the most remarkable new result is the universal relation between the scaled phase and the reduced distance from the center of the film. Given close similarities between these patterns and those in Rayleigh-Bénard convection with a similar aspect ratio [5], Γ emerges as a good indicator of spatiotemporal dynamics in systems where boundaries play an important role. The main qualitative difference is that here the rotating electric field imposes the spiral patterns' hand while the system in [5] has no handedness.

We thank E. Chin and J. W. Goodby for 10E6. P. E. C. acknowledges receipt of a 1993 John Simon Guggenheim Fellowship. H. R. B. acknowledges partial support of his work by the Deutsche Forschungsgemeinschaft.

[1] P. Manneville, *Dissipative Structures and Weak Turbulence* (Academic Press, New York, 1990).

[2] M. C. Cross and P. C. Hohenberg, Rev. Mod. Phys. **65**, 853 (1993).

[3] *Spatio-Temporal Patterns in Nonequilibrium Complex Systems,* Proceedings Volume XXII in the Santa Fe Institute Studies in the Sciences of Complexity, edited by P. E. Cladis and P. Palffy-Muhoray (Addison-Wesley, Reading, MA, 1994).

[4] S. C. Müller, T. Plesser, and B. Hess, Science **230**, 661 (1985); S. C. Müller, P. Coullet, and D. Walgraef, Chaos **4**, 439 (1994).

[5] E. Bodenschatz, J. R. deBruyn, G. Ahlers, and D. S. Cannell, Phys. Rev. Lett. **67**, 3078 (1991); E. Bodenschatz, S. W. Morris, J. R. de Bruyn, D. S. Cannell, and G. Ahlers, in *Pattern Formation in Complex Dissipative Systems,* edited by S. Kai (World Scientific, Singapore, 1992), p. 227.

[6] S. W. Morris, E. Bodenschatz, D. S. Cannell, and G. Ahlers, Phys. Rev. Lett. **71**, 2026 (1993).

[7] M. Assenheimer and V. Steinberg, Phys. Rev. Lett. **70**, 3888 (1993); Nature (London) **367**, 345 (1994).

[8] P. E. Cladis, J. T. Gleeson, P. L. Finn, and H. R. Brand, Phys. Rev. Lett. **67**, 3239 (1991).

[9] H. R. Brand and P. E. Cladis, Phys. Rev. Lett. **72**, 104 (1994).

[10] P. E. Cladis, A. J. Slaney, J. W. Goodby, and H. R. Brand, Phys. Rev. Lett. **72**, 226 (1994).

[11] P. E. Cladis, Y. Couder, and H. R. Brand, Phys. Rev. Lett. **55**, 2945 (1985).

[12] I. Mutabazi, P. L. Finn, J. T. Gleeson, J. W. Goodby, C. D. Andereck, and P. E. Cladis, Europhys. Lett. **19**, 391 (1992).

[13] Y. Couder, H. R. Brand, and P. E. Cladis (unpublished).

[14] P. E. Cladis and S. Torza, Phys. Rev. Lett. **35**, 1283 (1975).

[15] F. Kremer, S. U. Vallerien, H. Kapitza, and R. Zentel, Phys. Lett. A **146**, 273 (1990).

[16] G. Hauck and H. D. Koswig, Ferroelectrics **122**, 253 (1991).

[17] T. Frisch, S. Rica, P. Coullet, and J. M. Gilli, Phys. Rev. Lett. **72**, 1471 (1994); J. M. Gilli, M. Morabito, and T. Frisch, J. Phys. II (France) **4**, 319 (1994); K. B. Migler and R. B. Meyer, Physica (Amsterdam) **71D**, 412 (1994), and references therein.

[18] P. E. Cladis, P. L. Finn, and H. R. Brand (to be published).

[19] P. Keller, P. E. Cladis, P. L. Finn, and H. R. Brand, J. Phys. (Paris) **46**, 2203 (1985).

[20] As refractive indices are only approximately known in smectic C, the uncertainty in d is ~20%. These measurements were typically made without an applied voltage U while in the experiment $U \neq 0$.

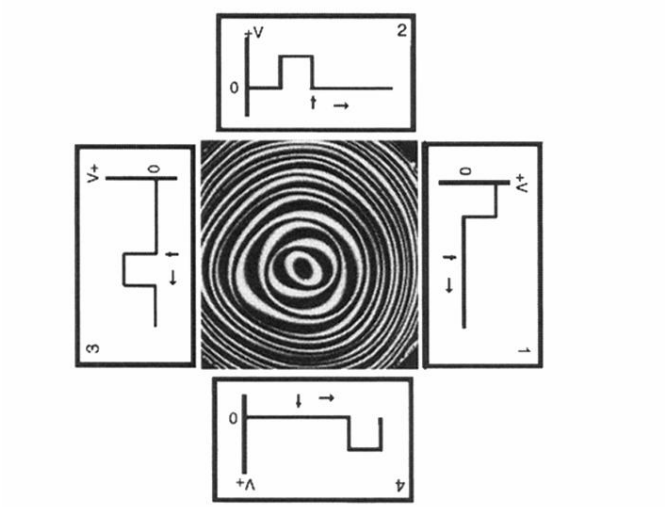

(a)

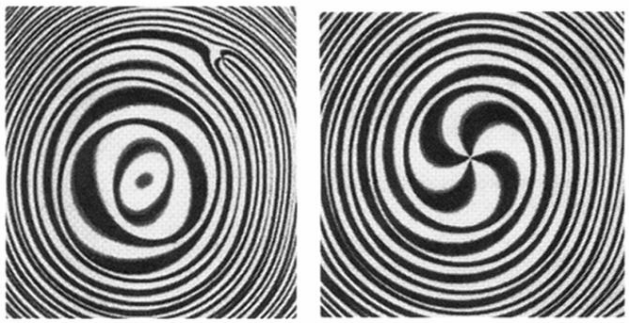

(b) (c)

FIG. 1. Basic steady-state patterns observed in thick freely suspended smectic-C films in a rotating electric potential U, $40 \lesssim U \lesssim 240$ V. Polarizer and analyzer are crossed parallel to the electrodes. (a) Experimental setup showing the electrode configuration and the applied voltage pulses: for a counterclockwise rotation, pulses applied to terminals 1 and 3 are $-90°$ out of phase with those to terminals 2 and 4. For the target state shown in the setup $d = 16$ μm, $U = 70$ V and scale, 1.3 mm (vertical) $\times$ 1.4 mm (horizontal). (b) Coexistence of an orbiting $S = +1$ defect and a target. The defect rotation sense is here counterclockwise, the same as the applied rotating field. A 2π rotation of the defect generates 2π more phase then propagates to the film center and is annihilated by the target: the target acts as a phase sink and the defect as a phase source. $d = 17$ μm, $U = 90$ V. the radial distance between the target center and the orbiting defect is 0.58 mm. (c) The $S = +1$ spiral ($U = 60$ V, $d = 17$ μm) with the orbiting defect in (b) at the film center. Same magnification as (b).

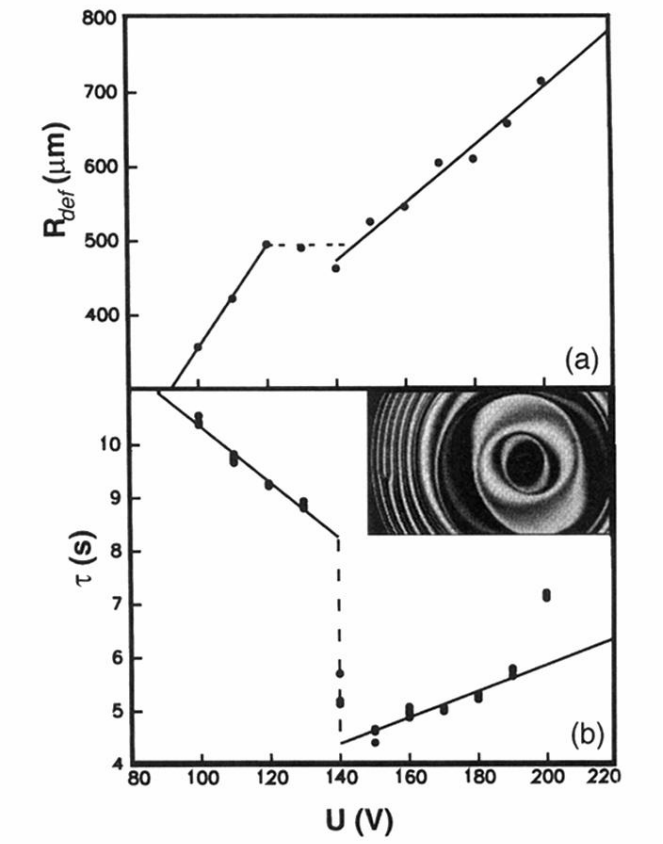

FIG. 4. (a) The orbit radius R_{def} and (b) the orbit time τ of the stationary bound state of an orbiting defect ($S = +1$) and target sink as a function of the applied voltage U. Inset in (b), a video frame of this stationary state shows only $\sim 2\pi$ phase in the inside region when $d = 13.5$ μm, $\nu = 2.6$ Hz, and $U = 200$ V. At $U = 240$ V, there is a transition to a chaotic state.